ARTICLE IN PRESS

Nature Communications

https://doi.org/10.1038/s41467-026-69054-3

Article in Press

Regulating interfacial water for oxygen transfer to benzylic C(sp^3)–H bonds via Ni-activated tungsten-oxygen covalency

Received: 8 October 2025

Accepted: 25 January 2026

Bing-Liang Leng, Xiu Lin, Hou-Yan Dong, Qi-Yuan Li, Shi-Nan Zhang, Jie-Sheng Chen & Xin-Hao Li

Cite this article as: Leng, B.-L., Lin, X., Dong, H.-Y. *et al.* Regulating interfacial water for oxygen transfer to benzylic C(sp^3)–H bonds via Ni-activated tungsten-oxygen covalency. *Nat Commun* (2026). https://doi.org/10.1038/s41467-026-69054-3

We are providing an unedited version of this manuscript to give early access to its findings. Before final publication, the manuscript will undergo further editing. Please note there may be errors present which affect the content, and all legal disclaimers apply.

If this paper is publishing under a Transparent Peer Review model then Peer Review reports will publish with the final article.

ARTICLE IN PRESS

© The Author(s) 2026. **Open Access** This article is licensed under a Creative Commons Attribution-NonCommercial-NoDerivatives 4.0 International License, which permits any non-commercial use, sharing, distribution and reproduction in any medium or format, as long as you give appropriate credit to the original author(s) and the source, provide a link to the Creative Commons licence, and indicate if you modified the licensed material. You do not have permission under this licence to share adapted material derived from this article or parts of it. The images or other third party material in this article are included in the article's Creative Commons licence, unless indicated otherwise in a credit line to the material. If material is not included in the article's Creative Commons licence and your intended use is not permitted by statutory regulation or exceeds the permitted use, you will need to obtain permission directly from the copyright holder. To view a copy of this licence, visit http://creativecommons.org/licenses/by-nc-nd/4.0/.

Regulating interfacial water for oxygen transfer to benzylic C(sp^3)–H bonds via Ni-activated tungsten-oxygen covalency

Authors: Bing-Liang Leng[1], Xiu Lin[1], Hou-Yan Dong[1], Qi-Yuan Li[1], Shi-Nan Zhang[1], Jie-Sheng Chen[1] and Xin-Hao Li[1]*

Affiliations:

[1]State Key Laboratory of Synergistic Chem-Bio Synthesis, School of Chemistry and Chemical Engineering, Shanghai Jiao Tong University, Shanghai 200240, People's Republic of China.

*Correspondence to: xinhaoli@sjtu.edu.cn (X.-H. L.)

Abstract

Recent studies on the electrocatalytic oxygen transfer from water to organic compounds have gained significant attention due to their sustainability and selectivity. However, the direct coactivation of inert hydrocarbons and water typically requires high oxidation potentials, leading to oxygen evolution reactions and low Faradaic efficiencies. Herein, a Ni-activated tungsten-oxygen covalency anode is designed for the efficient oxygen transfer from water to benzylic C(sp^3)–H bonds via the Ni-regulated interfacial water structure between the anode and electrolyte. Both experimental and theoretical results reveal the critical role of W–O covalency sites with Ni-heteroatoms for boosting efficient oxygen transfer via breaking the dense interfacial hydrogen bond network and inhibiting the undesired oxygen evolution reactions, facilitating the coactivation of oxygen species and C(sp^3)–H bonds. Thus, a Faradaic efficiency of > 56% in a water-involved system has been achieved. This work provides important insight into designing electrocatalytic systems for inert C–H oxidation.

Introduction

The production of functional oxygenated compounds via the activation of hydrocarbons using various oxidants accounts for approximately one-quarter of all industrial catalytic processes.[1,2] Moreover, over 30% of cradle-to-gate greenhouse gas emissions in chemical production can be attributed to the intensive energy input and uncontrolled overoxidation associated with traditional thermochemical methods.[3,4] Recent works on the electrocatalytic oxidation of hydroxyl/carbonyl groups[5–7], hydroxyl/carbonyl-α C–H bonds[8,9], various types of biomasses[10–14] and abundant hydrocarbons[15–17] have demonstrated the significant potential of using water molecules as a sustainable oxygen source[18,19] to produce functional organic compounds. However, the direct coactivation of even inert hydrocarbons and H_2O typically requires relatively high oxidation potentials[19,20], often leading to undesirable competitive oxygen evolution reactions (OER) and overoxidation, resulting in the formation of acids and esters[16,17], among other products. Though several works have put forward strategies such as electron density regulation[21], oxophilicity tuning[22–24], halogen mediation[25,26], and electrolyte engineering[27,28], et al. for facilitating the oxidation of olefins while depressing the OER process and overoxidation, the activation of even inert $C(sp^3)$–H bonds is still suffering from unsatisfied Faradaic efficiencies[15–17] (FE ~31%) especially in additive-free catalytic systems due to ultra-high oxidation potentials of inert $C(sp^3)$–H bonds as compared with that of OER. It is still highly alluring to put forward efficient strategies for activating $C(sp^3)$–H bonds for effective K/A oil production while inhibiting the OER process in an additive-free electrocatalytic system.

Herein, we show that Ni-activated tungsten-oxygen covalency (Ni-WOC) can efficiently boost the oxygen transfer from water to inert benzylic $C(sp^3)$–H bonds via loosening the originally dense interfacial water structure and promoting the $C(sp^3)$–H bond activation on the *in-situ* formed tungsten-oxygen covalency, effectively producing ketones and alcohols without overoxidation products (e.g., acids and esters). A reconstruction method is suggested to prepare highly dispersed and amorphous WOC sites with better catalytic performance than crystalline WO_3. Enabled by favorable lattice matching that ensures the reconstruction durability, the synergy between the Ni dopants and reconstructed WOC sites can largely disrupt the interfacial hydrogen bond network and simultaneously boost the co-activation of water molecules and C–H bonds. *In-situ* attenuated total reflection surface-enhanced infrared absorption spectroscopy (ATR-SEIRAS), *ab initio* molecular dynamics (AIMD), and density functional theory (DFT) studies reveal the critical role of Ni dopants in weakening the hydrogen bond network over the adjacent Ni-WOC species for faster oxygen transfer from water to substrates, simultaneously depressing the unwanted OER process via regulating the reaction path. Concurrently, the efficient oxidation of C(sp^3)–H bonds is achieved by the coactivation of C(sp^3)–H bonds and adsorbed oxygen on certain W sites of Ni-WOC. The combination of theoretical and experimental results demonstrates the boosted oxygen transfer process from water to C(sp^3)–H bonds on W–O covalency via the rationally introduced Ni heteroatoms, providing a Faradaic efficiency up to > 56% (Table S2).

Results

Oxygen transfer from water to benzylic C(sp^3)–H bonds

To introduce uniformly dispersed Ni dopants, we employed a carbothermal method to synthesize the Ni-doped tungsten carbide[29] (Ni/W_2C) pre-catalyst by thermal pyrolysis of the mixture of ammonium metatungstate, nickel nitrate hexahydrate, and dicyandiamide, in N_2 atmosphere at 1000 °C (for experimental details, please see supporting information). The Ni contents of Ni/W_2C samples can be precisely tuned from 0 via 0.8 and 1.6 to 3.1 wt.% by varying the amounts of nickel nitrate hexahydrate in the precursor (Table S1). With the increased Ni content from 0 wt.% to 3.1 wt.%, the as-formed tungsten carbide samples all exhibited similar structures of crystalline nanoclusters supported on layered graphene with mean sizes of 3.4-3.7 nm (Figure 1a and S1). Accordingly, the characteristic X-ray diffraction (XRD) peaks (Figure S2) of the (0 0 2) facet of α-phase W_2C (JCPDS# 35-776) [29–31] gradually shifted from 38.1° to 38.6°, indicating more Ni dopants were introduced to the crystal lattice of W_2C. Indeed, the uniformly dispersed Ni dopants in the crystal lattice of W_2C nanoclusters have been directly revealed by the aberration-corrected high-angle-annular-dark-field scanning transmission electron microscopy (AC-HAADF-STEM) (Figure 1a) with distinguishable differences in contrast of W and Ni atoms[32] in atomic resolution

AC-HAADF-STEM images (Figure 1b-c). The homogeneous dispersion of Ni dopants in W_2C clusters was further confirmed by corresponding energy-dispersive X-ray spectroscopy (EDS) mapping and line scan results (Figure 1a and S3-4). X-ray photo-electron spectroscopy (XPS) analysis results (Figure 1d and S5) further confirmed the presence of W and Ni atoms mainly in the form of metallic state, aligning well with the typical electronic configuration of transition metal carbides[29,33,34].

The as-obtained Ni/W_2C samples were investigated as potential anode pre-catalysts for the oxygenation of benzylic C(sp^3)–H bonds on ethylbenzene via oxygen transfer from water, which is utilized as a model reaction (Figure 2a) in a homemade undivided three-electrode system (for experimental details, please see Methods section). In this system, no oxygenated products were generated without an applied bias (Figure S6), regardless of whether Ni/W_2C was used as a pre-catalyst or not. At 1.8 V vs. Ag/AgCl, the system without pre-catalysts (Figure S6) could only exhibit very low yield (< 3%) and FE (< 17%). However, all Ni/W_2C pre-catalysts with different Ni contents (Figure S6) have exhibited higher yields (from 7.8% to 10%) and FEs (from 42.3% to 45.4%) at fixed conditions within 2 hours. More importantly, with optimized Ni content, the $Ni_{1.6}/W_2C$ pre-catalyst can successfully achieve the continuous oxygenation of benzylic C(sp^3)–H bonds with a yield up to 90% within 48 hours and a regio-selectivity of > 99% to 1-Phenylethanol and acetophenone (Figure 2b and S7), indicating an efficient electrocatalytic oxygen transfer process. The $Ni_{1.6}/W_2C$ pre-catalyst with optimized Ni content was employed for further studies.

It should be noted that the conversion and FE for oxygenated products are closely tied to the catalyst loadings (Figure 2c), highlighting the essential role of anode catalysts in facilitating the electrocatalytic oxygen transfer process. Moreover, this oxygen transfer process can be efficiently achieved over a broad range of working potentials (Figure 2d), from 1.6 V to 2.2 V (vs. Ag/AgCl), with satisfactory FE ranging from 47% to 56% (Figure 2d). And the FE of 56.5% under optimized conditions (Figure 2c-d and S8) is among the highest ones (Table S2) in currently all reported additive-free inert C(sp^3)–H oxidation system using water as oxygen source, indicating more favorable oxygenation process compared with OER pathway with a FE > 50%.

The isotope labeling experiments (Figure 2e) using $H_2{}^{18}O$ have further confirmed an efficient oxygen transfer process from water to C(sp^3)–H bonds, with only ^{18}O-labeled products detected (Figure 2f-g and S9). All these results reveal an electrocatalytic oxygen transfer process from water to C(sp^3)–H bonds, as depicted in Figure 2a.

***In-situ* formation of Ni-activated W–O covalency sites**

Interestingly, the progressive activation behavior (Figure 2b inset) of the pre-catalyst was observed at the earlier stage of the oxygenation reaction of ethylbenzene, manifested by a notable enhancement in catalytic activity. We thus turned our interest to the identification of real active sites. AC-HAADF-STEM images and the corresponding EDS mapping results of the used catalysts (Figure 3a) show highly dispersed and amorphous structures of W and Ni species (Figure 3b), rather speaking for a reconstruction process of the W_2C components to generate the real catalytic centers. The atomic-resolved AC-HAADF-STEM image (Figure 3c) of the reconstructed sample directly demonstrates the homogeneous distribution of Ni atoms over amorphous clusters, which shows the replacement of W to Ni atoms with obvious contrast difference (Figure 3d) and the comparable Ni/W–W distance without obvious loss of Ni sites in amorphous clusters. The fast degradation of metal carbide nanocrystals into an amorphous state within around 10 minutes was further revealed by the *ex-situ* X-ray diffraction (XRD) analysis (Figure S10).

The *ex-situ* XPS studies further suggested a migration process of oxygen species (Figure 3f) to generate WOC or Ni-WOC with W^{6+} (36.1 eV and 38.3 eV) or Ni^{2+} (856.5 eV) centers[29,31,35–38] from original metallic W^0 and Ni^0 states (Figure 3g-h and Table S3) respectively. Typical peaks of adsorbed hydroxyl groups[36,39–41] centered at 532.5 eV (Figure 3f) gradually decreased with prolonged reaction times, suggesting an oxygen transformation/transfer process from pre-adsorbed hydroxyl species to lattice oxygen for the formation of Ni-WOC, with lattice oxygen signal[35,36,40,42] (530.8 eV) becoming dominant after 10 minutes. Specifically, at the initial stage of the reaction (1 minute), a significant accumulation of hydroxyl groups at W sites was observed (Figure 3f), serving as the primary oxygen source for the formation of lattice oxygen in the WOC structure. From 1 minute to 30 minutes, the ratio of lattice oxygen increased from 21 % to 41% (Figure 3f), while the peak area of hydroxyl groups remained relatively constant (Figure 3f). This indicates an ongoing oxygen species migration process where hydroxyl groups transform into lattice oxygen, converting carbide into oxide, and the consumed hydroxyl groups can be readily replenished from the electrolyte, ensuring a continuous and abundant oxygen supply throughout the reaction period. Indeed, the potential-dependent *in-situ* Raman spectra and the *ex-situ* Raman spectra of the reconstructed samples confirmed the formation of tungsten-oxygen species (Figure S11) according to the ever-weakened W–C signal[43] from 690 cm^{-1} to 810 cm^{-1} and the accumulation of W=O signal[40,43–45] at around 940 cm^{-1}, as well as the W–O–W signal[45] at around 330 cm^{-1}. All these results, that the co-retention of Ni and W sites in amorphous clusters and the significant emergence of lattice oxygen, indicate the oxygen species-migration process as depicted in Figure 3e for the *in-situ* formation of Ni-WOC as the possible real active sites for the oxygen transfer process.

The *in-situ* generated highly dispersed Ni-WOC sites have provided fully exposed active sites with the essential synergy between WOC sites and uniformly dispersed Ni heteroatoms, which is of key importance for boosting the oxygen transfer process. Specifically, the yield (3.5 %) and FE (24.3%) toward oxygenated products on crystalline WO_3 (c-WO_3, Figure 3i and S12) anode is slightly lower than those of pristine WOC (4.0 % yield, 33.9% FE) or Ni/NC (3.7 % yield, 27.3% FE) anodes, indicating a slightly promoted oxygen transfer reaction on highly dispersed WOC or Ni sites. More importantly, the Ni-WOC anode could provide a yield of 10% and an FE of 45.4% under fixed conditions (Figure 3i and S12), which is 2.5 times the yield of the WOC anode and 2.1 times the yield of the mechanical mixture of WOC and Ni/NC. The decreased electrochemical surface area (ECSA) of Ni-WOC catalysts from 43.63 $mF\cdot cm^{-2}$ before reconfiguration to 25.01 $mF\cdot cm^{-2}$ after reconfiguration (Figure S13) rules out the influence of ECSA on the enhanced catalytic efficiency. The well-maintained layered graphene-supported structures after reconfiguration (Figure S14) further validate the unique role of Ni dopants, rather than any morphological changes in support, in enhancing the final catalytic performance. All these results reveal the essential importance of the *in-situ* formation process for highly dispersed Ni-WOC sites with obvious synergy between Ni heteroatoms and WOC sites for the enhanced oxygen transfer process, which cannot be solely attributed to the existence of tungsten oxides or the changes in surface area.

Boosted water diffusion over Ni-activated W–O covalency

The involvement of oxygen transfer in the formation of Ni-WOC also plays a crucial role in the subsequent oxygenation reaction, in which the arrangement of water molecules (the oxygen sources) at the interface between the Ni-WOC surface and electrolyte dominates the initial oxygen diffusion[46,47] efficiencies. The AIMD simulation results (Figure 4a-c, S15, and Supplementary Data 1-4) theoretically indicated the weakened hydrogen bond (H-bond) networks (Figure 4a-b) over the surface Ni sites of the Ni-WOC model, manifested by the decreased number of H-bonds from 4.8 on the WOC model to 2.9 on the Ni-WOC model in the area with a vertical distance (***z***) of 3.36 Å from the surface Ni atoms. This is to say that there is a void in the water layer over Ni sites as reflected by the absence of interfacial water (Figure 3c) in the domain with a radius (***r***) of 2.16 Å to Ni sites.

The loosened water network may benefit the penetration of water molecules through the Helmholtz layer to the Ni-WOC surface[48,49], as experimentally confirmed by ATR-SEIRAS analysis (Figure 4d). At a constant working potential of 2.0 V vs. Ag/AgCl, the non-hydrogen-bonded water signal[28,47,50,51] (at 3580 cm^{-1}) predominates in the interfacial water structure over the Ni-WOC-based anode throughout the reaction period (Figure 4d). In contrast, on the WOC-based anode, 2-coordinated hydrogen-bonded and 4-coordinated hydrogen-bonded water signals[28,47,50,51] (at around 3220 cm^{-1} and 3400 cm^{-1}) dominate during the reaction (Figure 4d). The increased ratio of non-hydrogen-bonded water molecules over the Ni-WOC-based anode indicates an efficient diffusion process. It is noteworthy that, with a fixed and low concentration (0.05M) of ClO_4^- in all the experiments, the ATR-SEIRAS results (Figure S16) reveal negligible ClO_4^- signals[52,53] in the region around 1100 cm^{-1} on both WOC and Ni-WOC catalyst surfaces throughout the reaction period. To further assess the universality of Ni heteroatoms in regulating the interfacial water structure, we conducted in-situ ATR-SEIRAS experiments in electrolytes containing different anions including SO_4^{2-} and HPO_4^{2-} (Figure S17). The population of weakly hydrogen-bonded water molecules on the Ni-WOC-based electrode surface increased significantly by factors of 1.63, 1.43 and 1.56 in $LiClO_4$, K_2HPO_4 and K_2SO_4 electrolytes, respectively, as compared to those on the WOC-based electrode (Figure S18). These results further confirm the dominant role of Ni dopants in regulating the interfacial water structure, rather than the influence of anions. More importantly, potential-dependent distribution of relaxation times (DRT) spectra (Figure 4e-f and S19) directly demonstrated the depressed diffusion resistance of oxygen species[54,55] from 392.8 Ω (at 0.8 V vs. Ag/AgCl) over the WOC-based anode (Table S4) to 336.1 Ω over the Ni-WOC-based anode. All these results unveil the critical role of Ni heteroatoms in breaking the originally dense interfacial H-bond network over the Ni-WOC surface and ensuring a fast oxygen diffusion process from electrolyte to adsorption sites on Ni-WOC, as depicted in Figure 4g.

Mechanism of oxygen transfer over Ni-activated W–O covalency

We then investigated the role of Ni in modulating the active sites for pre-adsorption and activation of water molecules transferred from the electrolyte to the Ni-WOC surface. Density functional theory (DFT) calculation results (Figure S20-22, Figure5a-b, and Supplementary Data 5-6) reveal an upward shift in the d-band center of metal sites (Figure S20) from –1.959 eV (WOC) to –1.902 eV (Ni-WOC) upon Ni doping. The Bader charge (Figure S21a-c) and differential charge density analysis results (Figure S21d) further demonstrate the role of Ni heteroatom as electron acceptor to attract 0.22 e^- from the adjacent WOC site (1 in Figure 5a). Accordingly, the W (1 in Figure 5a) atom adjacent to the Ni atom of the Ni-WOC model has the strongest coupling interaction with the pre-adsorbed water molecule with an adsorption energy of –0.921 eV (Figure 5b and Figure S22). The RDF between the claimed W1 atom and water molecules (Figure S23) also confirms the hydrophilic nature of this site with a W–O distance of 2.25 Å, consistent with the calculated adsorption energy (Figure 5b). It should be noted that the Ni site is not a favorable absorption site for water molecules with an adsorption energy of 0.085 eV, matching well with the trend of water affinity revealed by the AIMD simulation results (Figure 4a-c).

We further investigated the possible active oxygen species that might be derived from water for the subsequent oxygenation of C(sp^3)–H bonds. The isotope reaction using D_2O as the oxygen source (Figure 5c and S24a-b) could not provide deuterated products even with a reaction time of

4 hours, excluding the direct participation of hydroxide species (*OH) or oxyhydroxide species (*OOH) during the oxygen transfer process. Another control reaction using ^{18}O labeled Ni-WOC as the anode electrocatalyst could not give detectable amounts of ^{18}O-labeled products (Figure 5d and S24c-d), rather speaking for the absorbed oxygen (*O) from water activation rather than the lattice oxygen (O_{lat}) as the majority of the oxygen species for oxygen transfer process over the Ni-WOC anode. This result that *O plays as active species for inert bonds activation is consistent with previously reported cases[18,56].

After determining the adsorption site and the forms of possible active oxygen species, we turned our focus to the following coactivation of oxygen species and $C(sp^3)$–H bonds on the Ni-WOC anode. The gradually enhanced ATR-SEIRAS signals (Figure 5e) of hydrated tungstate[57] (centered at 1746 cm^{-1}), distinct from regular water bending modes (Figure S25), observed on Ni-WOC anode at ever-enlarged working potentials higher than 1.0 V (vs. Ag/AgCl) demonstrated a more favorable diffusion process of oxygen species to Ni-WOC anode surface as compared to bare WOC anode. With a similar trend of potential induced enhancement on the pre-adsorption of ethylbenzene[58,59] (Figure 5f), the Ni-WOC anode could directly trigger the transfer of oxygen to ethylbenzene via the formation of W–O–C bridge according to a more pronounced ATR-SEIRAS signal at around 1240 cm^{-1} of ethyl α-C bonded to metal through oxygen[60] (Figure 5g) on Ni-WOC anode. The potential-dependent blue shift of W–O–C signal from 1240 cm^{-1} at 1.0 V (vs. Ag/AgCl) to 1246 cm^{-1} at 2.4 V (vs. Ag/AgCl) further indicates an intensive electrocatalyzed oxygen transfer process, which contrasts sharply with rather weak W–O–C and unactivated $–CH_2–$ (1214 cm^{-1}) signals[58,59] on the WOC anode. To further validate the proposed oxygen transfer process, we conducted potentiostatic *in-situ* ATR-SEIRAS experiments at 2.0 V versus Ag/AgCl both before and after the addition of ethylbenzene (Figure 5h-j) to track the emergence of key intermediates. The ever-existing signals of hydrated tungstate[57] at 1746 cm^{-1} both before and after the addition of ethylbenzene (Figure 5h) indicate the strong affinity of W sites for water, facilitating subsequent water activation. Additionally, an emergent band corresponding to the C–C stretching mode of ethylbenzene[58,59] near 1040 cm^{-1} after the addition of ethylbenzene (Figure 5j) further confirms the efficient adsorption of ethylbenzene on Ni-WOC. Following the facile adsorption of water and ethylbenzene, the emerged signals at the region near 1246 cm^{-1} after adding ethylbenzene (Figure 5i) have indicated a C–H activation process through the formation of W–O–C structure[60]. Collectively, the Ni heteroatoms boost facile water adsorption (Figure 5e and Figure 5h) on neighboring W sites and thus promote C–H activation by forming W–O–C intermediate (Figure 5g and Figure 5j) on Ni-WOC-based electrode. These results indicate that the oxygen transfer process is induced by the coactivation of water and C–H bonds boosted by Ni heteroatoms, while the formation of the W–O–C structure plays as a key intermediate in the oxygen transfer process.

Theoretically, we further investigated the possible role of Ni-WOC in regulating reaction pathways from OER to oxygenation of C(sp^3)–H bonds. As revealed by DFT calculations (Figure 5k, S26-27, and Table S5-6), the energy barrier of each step for the formation of *O as active oxygen species on the Ni-WOC model has decreased dramatically. The DRT spectra also indicate improved reaction kinetics, corresponding to a timescale of 10^{-3} s at the cathode upon introducing Ni dopants (Figure S28 and Table S7). The kinetic impedance is reduced to 8.0 Ω for the Ni-WOC catalyst, compared to 14.0 Ω for the WOC catalyst (Table S7). The integration of theoretical and experimental results highlights the crucial role of Ni dopants in efficiently activating water molecules for generating active oxygen species from an intrinsic kinetics perspective. However, as the DFT calculation suggested, the ΔG value for the hydroxylation step from *O to *OOH as the rate-determining step (RDS) for OER has increased from 3.02 eV on the WOC model to 3.33 eV on the Ni-WOC model. Experimentally, the suppression of OER by Ni doping is directly evidenced by the decrease in FE for O_2 from 55.2% on the WOC-based electrode to 34.1% on the Ni-WOC-based electrode (Figure S29). More importantly, the ΔG value for the adsorption of ethylbenzene with the formation of *O on the Ni-WOC model is as low as 2.83 eV, making it more favorable for the oxygenation of C(sp^3)–H bonds rather than the formation of *OOH from *O in OER. The displacement of OER by ethylbenzene oxidation is further experimentally manifested by linear sweep voltammetry curves (Figure S30a), where both the appearance of a distinct oxidation peak at 1.72 V (vs. Ag/AgCl) and a simultaneous decrease in the OER current after adding ethylbenzene into original water-based electrolyte were observed. Additionally, isotope kinetic effect (KIE) was also tested to reveal the changes of the rate-determining step (Figure S30b-d). The calculated KIE value (j_H/j_D, j_H: the current density measured in H_2O-based electrolyte, and j_D: the current density measured in D_2O-based electrolyte) at 1.72 V (vs. Ag/AgCl) decreases from 1.40 (OER alone) to 1.22 (with ethylbenzene), indicating that the isotopic effect of water oxidation becomes less dominant when C–H activation and oxidation are involved. All these results have clearly elucidated the essential role of Ni heteroatoms in boosting the coactivation of water and C(sp^3)–H bonds while suppressing the undesired OER process (from *O to *OOH) from an intrinsic kinetics perspective, well explaining the high FE values for producing oxygenated compounds as supported by both theoretical and experimental evidence.

Performance of electrocatalytic oxygen transfer reaction

Taken together, the Ni heteroatoms regulate interfacial water structure for fast oxygen diffusion from electrolyte to Ni-WOC surface, simultaneously boosting the coactivation of oxygen species and C(sp^3)–H bonds on W–O covalency sites with inhibited OER process. In this way, the Ni-WOC-based anode has provided satisfactory FEs ranging from 43.2% to 64.8% in a general scope of benzylic C(sp^3)–H bonds (Figure 6a), including secondary (Ethylbenzene, Propylbenzene) and tertiary (iso-Propylbenzene, Diphenylmethane) C(sp^3)–H bonds with electron-withdrawing (3-Ethyl-Fluorobenzenen) or donating (*o*-Ethyltoluene, *p*-Ethyltoluene) groups. It should be noted that the current substrate scope is still limited to benzylic C(sp^3)–H bonds and the near-unity regioselectivity is governed by the inherent reactivity of the benzylic site itself, requiring further research to expand this promising oxygen transfer system.

Additionally, Ni-WOC-based anode has provided durable capability for oxygen transfer from water to C(sp^3)–H bonds with high FEs (from 55.2% to 58.4%) for oxygenated products (Figure 6b) without obvious decay in catalytic performance for more than 6 circles of reuse. More importantly, after a long-term electrolysis, the Ni-WOC structure remains durable with abundant amorphous features revealed by TEM (Figure S31a-b) and XRD (Figure S32). XPS analysis indicates a raised Ni^{2+}/Ni^0 ratio from 0.15 to 10.11 and W^{6+}/W^0 ratio from 0.37 to 21.22 (Figure S33a-b and Table S3), along with the significant emergence of lattice oxygen (Figure S33c). The

EDS mapping (Figure S31e-f) confirms the homogeneous distribution of Ni atoms over the whole support of the spent catalyst. Quantitative EDS spectra (Figure S31d and Table S8 in the revised supplementary information) and the ICP-OES (Table S8) analysis results further demonstrate the consistent Ni/W atomic ratios before (0.095 via ICP-OES) and after (0.086 via ICP-OES and 0.107 via EDS) long-term uses, rather speaking for the co-retention of Ni-W complex during the long-term electrolysis.

Besides the excellent capability and durability, the Ni-WOC-based electrocatalytic devices utilizing water as an oxygen source for additive-free oxygenation of inert C(sp^3)–H bonds are competitive when compared with the state-of-the-art electrocatalytic systems reported in the literature[15,17,61–63] (Figure 6c and Table S2). Taking ethylbenzene as an example, the Ni-WOC-based anode has provided a satisfactory FE up to 58.4% (Figure 6c and Table S2). And a continuous oxygen transfer process for a high yield up to 90% has been achieved on Ni-WOC-based anode, which is among the competitive ones in the currently reported cases (Figure 6c and Table S2). Accordingly, the Ni-WOC-based anode has exhibited an energy efficiency (η_E) of 10.9 mol/kW·h (Figure 6c and Table S2). Additionally, the additive-free feature of the Ni-WOC anode has significantly reduced the costs associated with material and product purification (Figure 6c and Table S2).

Discussion

In summary, we have demonstrated the essential role of Ni-activated W–O covalency sites in boosting the oxygen transfer process from water to benzylic C(sp^3)–H bonds to produce K/A oil. Ni heteroatoms modulate the electronic deficiency of neighboring W sites, resulting in an enhanced oxygen transfer process which improves both mass transfer and intrinsic kinetics. Specifically, Ni heteroatoms disrupt the water structure at the anode/electrolyte interface, breaking the dense hydrogen bond network and facilitating the rapid diffusion of water molecules to the W–O covalency sites of Ni-WOC. Additionally, the coactivation of oxygen species and C(sp^3)–H bonds is enhanced at the W–O covalent sites adjacent to Ni heteroatoms, further promoting the effective oxygenation process. More importantly, the undesired OER process is inhibited by Ni heteroatoms via a regulated reaction pathway, thereby providing satisfactory FEs for effective C(sp^3)–H oxygenation reactions using water as an oxygen source in a general scope of substrates. This work not only highlights the importance of catalyst-tuned interfacial water structure for the oxidation of organic compounds but also provides important insights into designing electrocatalytic systems for inert C–H oxidation using water as the oxygen source.

Methods

Chemicals and materials

Ethylbenzene (C_8H_{10}, 99.0%), Water-^{18}O ($H_2{}^{18}O$, 98.0%), Deuterium Oxide (D_2O, 99%), Propylbenzene (C_9H_{12}, 99%), Sulfolane ($C_4H_8O_2S$, 99.0%), *p*-Ethyltoluene (C_9H_{12}, 98%), and *o*-Ethyltoluene (C_9H_{12}, 98%) were purchased from Adamas. iso-Propylbenzene (C_9H_{12}, 99%) and 1-Ethyl-3-Fluorobenzenen (C_8H_9F, 98%) were purchased from Macklin. Ammonium Metatungstate ($(NH_4)_6H_2W_{12}O_{40}\cdot xH_2O$, 99.5%), Nickel (II) Nitrate Hexahydrate ($Ni(NO_3)_2\cdot 6H_2O$, 99%), Urea (CH_4N_2O, 99.5%),1, 4-Benzenedicarboxylic Acid ($C_8H_6O_4$, 99%), Lithium Perchlorate ($LiClO_4$, 99.95%), Triethylene Diamine ($C_6H_{12}N_2$, 98%), and N,N-Dimethylformamide (C_3H_7NO, 99.5%) were purchased from Aladdin. Anisole (C_7H_8O, 99.0%) and Diphenylmethane ($C_{13}H_{12}$, 99.0%) were purchased from TCI. Potassium Hydroxide (KOH, 95%) and Ethanol (C_2H_5OH, 99.8%) were purchased from Greagent. Dicyandiamide ($C_2H_4N_4$, 99.5%) was purchased from Acros Organics. Nafion solution (5%) were purchased from DuPont. Nitrogen (N_2, 99.999%) and Argon (Ar, 99.999%) were purchased from Air Liquide. Carbon Cloth (W0S1002) was purchased from CeTech. All chemicals and materials were used as received without further purification.

Synthesis of Ni/W$_2$C and W$_2$C pre-catalysts

Synthesis of Ni/W$_2$C: Typically, 0.50 g ammonium metatungstate and 10.00 g dicyandiamide were mixed with different contents of nickel (II) nitrate hexahydrate (23.60 mg, 47.20 mg, 94.40 mg) in 50 mL deionized water. The mixture was heated at 80 °C under continuous stirring to remove the water. The as obtained homogeneously solid mixture with light green color was grinded into powder and transferred into a cylindrical crucible with a lid. The crucible with the precursor was heated at 1000 °C for 2 hours with a heating rate of 2.5 °C min^{-1} under a highly pure nitrogen gas atmosphere. The final product was collected after naturally cooling down and denoted as $Ni_{0.8}/W_2C$ (with 23.60 mg nickel nitrate hexahydrate), Ni/W_2C (with 47.20 mg nickel nitrate hexahydrate), $Ni_{3.1}/W_2C$ (with 94.40 mg nickel nitrate hexahydrate) respectively.

Synthesis of W_2C: The synthesis of W_2C follows the same procedure as that of Ni/W2C, with the exception that nickel nitrate hexahydrate is omitted from the precursor.

Synthesis of c-WO_3 catalysts

The crystalline WO_3 was synthesized by heating the monoclinic $WO_3 \cdot H_2O$ which was obtained by the Freedman method. Typically, 10 mL of 1 M $Na_2WO_4 \cdot 2H_2O$ was added into 90 mL of 3 M HCl. The as formed yellow mixture was stirred overnight at 300 rpm at the room temperature. The sample obtained was collected via vacuum filtration and washed with deionized water until the pH of the rinsed solution reached approximately 6. The obtained yellow powder was dried at 60 ℃ overnight to get the monoclinic $WO_3 \cdot H_2O$. The monoclinic WO_3 was obtained by heating $WO_3 \cdot H_2O$ at 350 °C for 5 hours in air with a heating rate of 5 °C min^{-1}. The final product collected after naturally cooling down was denoted as c-WO_3. The XRD patterns of the synthesized $WO_3 \cdot H_2O$ and WO_3 samples have demonstrated their crystalline structure as shown in Figure S2c-d.

Synthesis of Ni/NC catalysts

Briefly, the urea was heated to 550 °C for 4 hours in air with the heating rate of 2.3 °C/min to form the polymeric carbon nitride (PCN). 6.19 g PCN powder was mixed with homogeneous mixture of 48.7 mg nickel (II) nitrate hexahydrate, 0.91 g 1, 4-benzenedicarboxylic acid and 0.64 g triethylene diamine in N, N-dimethylformamide (DMF) solution. The resulting solid powder after removing solvent was heated to 900 °C for 1 hour with a heating rate of 1.5 °C/min under an N_2-protected atmosphere. The as-obtained black solid samples were denoted as Ni/NC.

Preparation of working electrodes

The catalyst ink was prepared by mixing 10 mg corresponding catalyst and a solution containing

300 μL Nafion solution (5%), 700 μL deionized water, and 1400 μL Ethanol. The obtained mixture was sonicated for 2 hours to get homogenous dispersed ink.

The working electrode was prepared by homogeneously dipping specific volumes of the ink onto a 2×2 cm^2 carbon cloth, followed by drying at 120 ℃ for 1 hour. The as obtained electrode was used for the further electrocatalytic test.

Electrocatalytic oxygen transfer reaction tests

All the electrocatalytic experiments were performed in a homemade undivided cell with a three-electrode system (Figure S33) on a potentiostat (CHI 660E, Shanghai CH Instruments Company). Working electrodes (the anode) were composed of catalysts supported on a carbon cloth. A Titanium (Ti) mesh with a size of 2×2 cm^2 and an Ag/AgCl electrode was employed as the cathode and reference electrode, respectively. For the oxygen transfer reaction, the potentiostatic test was conducted in an Ar-saturated electrolyte composed of water/sulfolane solution containing 25 mM ethylbenzene and 50 mM $LiClO_4$. The sulfolane was used as a bipolar solvent to improve the homogeneous dispersion of the ethylbenzene phase in the electrolyte. The influence of the volume ratio of sulfolane was shown in Figure S8.

The electrocatalytic continuous oxygen transfer reaction was conducted for continuous 48 hours without intervals. The electrocatalytic stability tests of electrodes for oxygen transfer reaction were evaluated via six repeated cycles at the same working potential with each cycle of 2 hours.

The generated anode products were analyzed by GC-MS (Shimadzu QP2010SE equipped with SH-Rxi-5Sil MS column) to determine the components of products and calculate the yield and Faradaic efficiency.

The Faradaic efficiency (FE) was calculated as follows:

$$\text{FE (\%)} = \frac{\sum N_i \times n \times F}{Q} \times 100\ \%$$

where N_i (mole) is the number of moles for the specific product (alcohols and ketones); n is the number of electrons exchanged for product formation, which is 2 for alcohols and 4 for ketones; F is the Faradaic constant of 96485 C mol^{-1}; Q is the measured passed charge.

The energy efficiency (η_E) was calculated as follows:

$$\eta_E\ (\text{mol kW}\cdot\text{h}^{-1}) = \frac{N}{W}$$

where N (mole) is the number of moles for the conversed substrates; W (kW·h) is the consumed electronic work during the electrocatalytic process.

Electrochemical active surface area measurement

The electrochemical active surface area (ECSA) of the catalysts both before and after the reconstruction were both measured in 0.1 M KOH electrolyte using cyclic voltammetry method. Working electrodes (the anode) were composed of catalysts supported on a 2×2 cm^2 carbon cloth. A Titanium (Ti) mesh with a size of 2×2 cm^2 and an Ag/AgCl electrode was employed as the cathode and reference electrode, respectively. For the fresh catalysts, the cyclic voltammetry was performed by scanning from 0.816 V (vs. Ag/AgCl) to 0.916 V (vs. Ag/AgCl) at scanning rates of 2, 4, 6, 8, 10, and 15 $\text{mV}\cdot\text{s}^{-1}$. The ECSA measurement for reconstructed samples follows the same procedure, with the exception that the working electrode was changed to a reconstructed one. The ECSA was calculated as follows:

$$\text{ECSA} = \frac{C_{dl}}{C_s}$$

where C_{dl} is the double layer capacitance measured from cyclic voltammetry method; C_s is the reference capacitance.

In-situ Raman spectroscopy studies

The *in-situ* Raman measurements were conducted on Renishaw inVia Qontor Raman microscope using a custom-designed *in-situ* electrochemical cell (Figure S34a). Specifically, the measurements were performed using a 532 nm semiconductor laser at 2.5 mW power and a 50× microscope objective, with frequencies calibrated against silicon wafers beforehand. The experiments utilized an undivided three-electrode cell equipped with an embedded quartz window. The electrode configuration consisted of a platinum wire counter electrode, an Ag/AgCl reference electrode, and a working electrode made from carbon cloth loaded with catalyst at 1 mg cm^{-2}. Water-sulfolane mixture (volume ratio of 3:1) with 25 mM ethylbenzene and 50 mM LiClO_4 was used as electrolyte. A potentiostat (Vertex.C, Ivium Technologies B.V.) was used to control the potential during the Raman test. Each spectrum in the *in-situ* potentiodynamic Raman test under different applied bias ranging from 0.4 V to 1.8 V (vs. Ag/AgCl) were collected for approximately 10 minutes every 0.2 V.

***In-situ* infrared absorption spectroscopy studies**

The attenuated total reflection surface-enhanced infrared absorption spectroscopy (ATR-SEIRAS) measurements were run on a Nicolet iS50 FTIR spectrometer equipped with a HgCdTe (MCT) detector using a custom-designed *in-situ* electrochemical cell (Figure S34b). All measurements are conducted at the Kretschmann configuration, incorporating an Au film-coated Si window with catalyst ink dropped on it. The Au film functions both as a current collector and a SEIRA-active substrate, enabling *in-situ* analysis of the anode/electrolyte interfaces close to the catalyst with high sensitivity. Water-sulfolane mixture (volume ratio of 3:1) with 25 mM ethylbenzene and 50 mM $LiClO_4$ was used as electrolyte, with an Ag/AgCl electrode and a Pt mesh as the reference electrode and cathode, respectively. The IR spectra were collected with p-polarized IR radiation at the spectral resolution of 8 cm^{-1}. The incidence angle is ca. 60°. All spectra were shown in the absorbance unit as $-\log(I/I_0)$, where I and I_0 represent the intensities of the reflected radiation for sample and reference single-beam spectra, respectively.

In-situ potentiostatic ATR-SEIRAS spectra for the surface water structure were collected continuously at working conditions (2.0 V vs. Ag/AgCl) every 2 minutes. The whole experimental period is 30 minutes.

In-situ potentiodynamic ATR-SEIRAS spectra for the oxygen transfer process at a scan rate of 5 $mV\cdot s^{-1}$ were continuously collected every 200 mV at the cell voltage from 0.2 to 2.4 V (vs. Ag/AgCl).

In-situ potentiostatic ATR-SEIRAS spectra for the oxygen transfer process at a constant working potential of 2.0 V vs. Ag/AgCl were continuously collected every 1 minute. The ethylbenzene was added into the *in-situ* electrochemical cell between 9 and 10 minutes.

Each single-beam spectrum was averaged of 32 scans, corresponding to a period of ca. 14 s. The concentration of $LiClO_4$ (50 mM) was fixed throughout all experiments to rule out the potential influence of anions for water structure.

Distribution of relaxation times analysis

Potentiostatic electrochemical impedance spectra (EIS) were collected in the range from 0.1 Hz to 1 MHz every 0.2 V at the bias ranging from 0.4 to 1.6 V (vs. Ag/AgCl) (see Figure S19). To determine the oxygen species diffusion process over Ni-WOC anode, 1 M KOH was used as the electrolyte. The distribution of relaxation times[64–66] (DRT) is used to analyze the EIS data.

DRT impedance, $Z_{\mathrm{DRT}}(f)$, at a frequency f, can be expressed as

$$Z_{DRT} = R_{\infty} + \int_{-\infty}^{\infty} \frac{\gamma(\ln\tau)}{1 + i2\pi f\tau} \mathrm{d}\ln\tau$$

Where R_{∞}, τ, $\gamma(\ln\tau)$ and f are the ohmic resistance, relaxation time, distribution function of relaxation time, and frequency respectively. Moreover, polarization resistance, R_{pol}, is computed by:

$$R_{pol} = \int \gamma(\ln\tau)\mathrm{d}\ln\tau$$

Density functional theory calculations

Density functional theory (DFT) calculations were conducted utilizing the Vienna Ab Initio Simulation Package (VASP)[67,68]. The generalized gradient approximation (GGA) with the Perdew-Burke-Ernzerh (PBE) of exchange-correlation functional[69] was employed. The DFT-D3 method[70,71] was employed to incorporate van der Waals interactions. A plane-wave expansion with a kinetic energy cutoff of 450 eV was employed. The convergence criteria for energy and force were set to 10^{-5} eV and 0.02 eV Å^{-1}, respectively. K-points were set to 3×3×1 for geometry optimization and energy calculation. A vacuum layer with a thickness of 15 Å along z-direction was applied to avoid unreasonable interactions among periodical images along z-direction.

The amorphous W–O covalency model was constructed by using *ab initio* molecular dynamics. Briefly, the originally crystalline Ni-doped WO_3 model was treated using *ab initio* molecular dynamics by VASP with all layers fully relaxed. The system was maintained at 600 K in an NVT ensemble framework to obtain the amorphous structure. The total duration of the AIMD simulation reached 5 ps.

The Gibbs free energy change for each step of the oxidation reaction was calculated as follows:

$\Delta G = \Delta E + \Delta \mathrm{ZPE} - T\Delta S$ (T = 298.15 K)

where ΔE, ΔZPE, and ΔS are the changes in the reaction energy, zero-point energy, and entropy, respectively. Each step and the corresponding ΔG values of the OER and oxygenation pathway are listed in Table S5-6.

***Ab initio* molecular dynamics simulation**

The *ab initio* molecular dynamics (AIMD) simulation for the structure of interfacial water over the Ni-WOC and WOC models were carried out using the open source CP2K/Quickstep package[72] based on a hybrid Gaussian plane wave (GPW) scheme. The orbitals are described by an atom centered Gaussian-type basis set. An auxiliary plane wave basis set with a cutoff energy of 400 Ry is used to re-expand the electron density in the reciprocal space. Perdew-Burke-Ernzerhof (PBE) functional[69] with DFT-D3 dispersion correction[70,71] was used. The core electrons were represented by analytic Goedecker-Teter-Hutter (GTH) pseudopotentials[73,74]. For valence electrons, the Gaussian basis sets were double-ζ basis functions with one set of polarization functions (DZVP)[75].

The initial model of catalyst/water interfaces were constructed using the previously obtained amorphous W–O covalency model for DFT calculations. The simulation cell was filled with 116 water molecules and a vacuum layer of approximately 20 Å in z-direction. The entire simulation cell has a size of 15.44×15.44×46.00 Å^3 as shown in Figure S15.

All AIMD simulations were performed in the NVT ensemble, with Nosé–Hoover chain thermostat[76] to keep a constant temperature of 298.15 K. A time step of 0.5 fs was adopted for the Velocity-Verlet algorithm[77]. The structural relaxation process lasted for 2 ps to obtain equilibrium configurations, followed by a simulation of 10 ps for the production process used for the final analysis. All the simulation was conducted in periodic boundary conditions.

The hydrogen bond analysis follows a typical criterion of a 30° angle cutoff and a 3.5 Å bond length cutoff. To ensure the accuracy of the simulation, all presented results are statistical averages calculated over a 10 ps simulation, corresponding to 20,000 steps. This extensive sampling effectively filters out any anomalous simulation artifacts. Additionally, simulations of both the Ni-WOC and WOC models were conducted under identical conditions, providing clear evidence of the disruption of hydrogen bond networks near the doped Ni sites.

Structural characterization

Aberration-corrected high-angle annular dark field scanning transmission (AC-HAADF-STEM) images were recorded on Hitachi HF5000 scanning/transmission electron microscope at an acceleration voltage of 200 kV with a probe spherical aberration corrector. The corresponding Energy Dispersive X-ray Spectra (EDS) were collected by an INCA X-Max 80 TEM EDS spectrometer. Transmission electron microscopy (TEM), high-resolution transmission electron microscopy (HRTEM) and HAADF-STEM images were recorded by a Talos F200X G2 microscope with an acceleration voltage of 200 kV. Powder X-ray diffraction (XRD) patterns were recorded on a Rigaku Miniflex 600C X-ray diffractometer with Cu Kα radiation (λ = 1.5418 Å) and operated at a scan rate of 5° min^{-1}. X-ray photoelectron spectroscopy (XPS) experiments were performed using a Kratos Axis Ultra DLD spectrometer with monochromated Al Kα radiation. The inductively coupled plasma atomic emission spectroscopy (ICP-AES) measurement was conducted on an iCAP6300 spectrometer for metal element analysis. The Raman spectroscopy was conducted on Renishaw inVia Qontor Raman microscope with the laser wavelength of 532 nm.

Data Availability

All the relevant data are included in this paper and its Supplementary Information. The data that supports the findings of this study are available from the corresponding authors upon request. Source data are provided with this paper.

References

1. Haber, J. Fundamentals of Hydrocarbon Oxidation. in *Handbook of Heterogeneous Catalysis* 3359–3384 (John Wiley & Sons, Ltd, 2008). doi:10.1002/9783527610044.hetcat0170.
2. Zheng, R., Liu, Z., Wang, Y., Xie, Z. & He, M. The future of green energy and chemicals: Rational design of catalysis routes. *Joule* **6**, 1148–1159 (2022).
3. Leow, W. R. *et al.* Electrified hydrocarbon-to-oxygenates coupled to hydrogen evolution for

efficient greenhouse gas mitigation. *Nat. Commun.* **14**, 1954 (2023).

4. Cullen, L., Meng, F., Lupton, R. & Cullen, J. M. Reducing uncertainties in greenhouse gas emissions from chemical production. *Nat. Chem. Eng.* **1**, 311–322 (2024).
5. Qin, Y. *et al.* Adjacent-Ligand Tuning of Atomically Precise Cu−Pd Sites Enables Efficient Methanol Electrooxidation with a CO-Free Pathway. *Angew. Chem. Int. Ed.* **64**, e202420817 (2025).
6. Shi, R. *et al.* Electrochemical oxidation of concentrated benzyl alcohol to high-purity benzaldehyde via superwetting organic-solid-water interfaces. *Sci. Adv.* **10**, eadn0947 (2024).
7. Tian, B. *et al.* Parameterization and quantification of two key operando physio-chemical descriptors for water-assisted electro-catalytic organic oxidation. *Nat. Commun.* **15**, 10145 (2024).
8. Li, Y. *et al.* Accelerated Selective Electrooxidation of Ethylene Glycol and Inhibition of C–C Dissociation Facilitated by Surficial Oxidation on Hollowed PtAg Nanostructures via In Situ Dynamic Evolution. *JACS Au* **5**, 714–726 (2025).
9. Shi, K., Si, D., Teng, X., Chen, L. & Shi, J. Pd/NiMoO4/NF electrocatalysts for the efficient and ultra-stable synthesis and electrolyte-assisted extraction of glycolate. *Nat. Commun.* **15**, 2899 (2024).
10. Zhang, N. *et al.* Electrochemical Oxidation of 5-Hydroxymethylfurfural on Nickel Nitride/Carbon Nanosheets: Reaction Pathway Determined by In Situ Sum Frequency Generation Vibrational Spectroscopy. *Angew. Chem. Int. Ed.* **58**, 15895–15903 (2019).
11. Gu, K. *et al.* Defect-Rich High-Entropy Oxide Nanosheets for Efficient 5-Hydroxymethylfurfural Electrooxidation. *Angew. Chem. Int. Ed.* **60**, 20253–20258 (2021).
12. Pei, A. *et al.* Enhanced electrocatalytic biomass oxidation at low voltage by Ni^{2+}-O-Pd interfaces. *Nat. Commun.* **15**, 5899 (2024).
13. Zhang, P. *et al.* Paired Electrocatalytic Oxygenation and Hydrogenation of Organic Substrates with Water as the Oxygen and Hydrogen Source. *Angew. Chem. Int. Ed.* **58**, 9155–9159 (2019).
14. Chi, H. *et al.* Electrosynthesis of ethylene glycol from biomass glycerol. *Nat. Commun.* **16**,

979 (2025).

15. Sun, Y. *et al.* Highly selective electrocatalytic oxidation of benzyl C–H using water as safe and sustainable oxygen source. *Green Chem.* **22**, 7543–7551 (2020).
16. Li, Z. *et al.* Electrocatalytic ethylbenzene valorization using a polyoxometalate@covalent triazine framework with water as the oxygen source. *Chem. Commun.* **57**, 7430–7433 (2021).
17. Seo, B. *et al.* Electrochemical oxidation of toluene with controlled selectivity: The effect of carbon anode. *Appl. Surf. Sci.* **534**, 147517 (2020).
18. Liu, C., Chen, F., Zhao, B.-H., Wu, Y. & Zhang, B. Electrochemical hydrogenation and oxidation of organic species involving water. *Nat. Rev. Chem.* **8**, 277–293 (2024).
19. Leng, B.-L., Lin, X., Chen, J.-S. & Li, X.-H. Electrocatalytic water-to-oxygenates conversion: redox-mediated versus direct oxygen transfer. *Chem. Commun.* **60**, 7523–7534 (2024).
20. Kawamata, Y. *et al.* Scalable, Electrochemical Oxidation of Unactivated C–H Bonds. *J. Am. Chem. Soc.* **139**, 7448–7451 (2017).
21. Lin, X. *et al.* Direct Oxygen Transfer from H_2O to Cyclooctene over Electron-Rich RuO2 Nanocrystals for Epoxidation and Hydrogen Evolution. *Angew. Chem. Int. Ed.* **61**, e202207108 (2022).
22. Dorchies, F. *et al.* Controlling the Hydrophilicity of the Electrochemical Interface to Modulate the Oxygen-Atom Transfer in Electrocatalytic Epoxidation Reactions. *J. Am. Chem. Soc.* **144**, 22734–22746 (2022).
23. Chung, M., Jin, K., Zeng, J. S., Ton, T. N. & Manthiram, K. Tuning Single-Atom Dopants on Manganese Oxide for Selective Electrocatalytic Cyclooctene Epoxidation. *J. Am. Chem. Soc.* **144**, 17416–17422 (2022).
24. Chung, M. *et al.* Direct propylene epoxidation via water activation over Pd-Pt electrocatalysts. *Science* **383**, 49–55 (2024).
25. Leow, W. R. *et al.* Chloride-mediated selective electrosynthesis of ethylene and propylene oxides at high current density. *Science* **368**, 1228–1233 (2020).
26. Gao, Y. *et al.* Membrane-Free Electrosynthesis of Epichlorohydrins Mediated by Bromine

Radicals over Nanotips. *J. Am. Chem. Soc.* **146**, 714–722 (2024).

27. Yao, J. *et al.* Interfacial Hydrogen-Bond Network Regulation Tuned Water Dissociation Enables Selective Chlorination of Alkenes. *J. Am. Chem. Soc.* **147**, 8024–8031 (2025).
28. Yan, M., Yang, R., Liu, C., Gao, Y. & Zhang, B. In Situ Probing the Anion-Widened Anodic Electric Double Layer for Enhanced Faradaic Efficiency of Chlorine-Involved Reactions. *J. Am. Chem. Soc.* **147**, 6698–6706 (2025).
29. Lin, X. *et al.* Electrochemical activation of C–H by electron-deficient W_2C nanocrystals for simultaneous alkoxylation and hydrogen evolution. *Nat. Commun.* **12**, 3882 (2021).
30. Pol, S. V., Pol, V. G. & Gedanken, A. Synthesis of WC Nanotubes. *Adv. Mater.* **18**, 2023–2027 (2006).
31. Yang, B. *et al.* Optimization of hydrogen adsorption on W_2C by late transition metal doping for efficient hydrogen evolution catalysis. *Mater. Today Nano* **23**, 100350 (2023).
32. Yan, J. *et al.* Single atom tungsten doped ultrathin α-$Ni(OH)_2$ for enhanced electrocatalytic water oxidation. *Nat. Commun.* **10**, 2149 (2019).
33. Goto, Y. *et al.* Formation of Ni_3C Nanocrystals by Thermolysis of Nickel Acetylacetonate in Oleylamine: Characterization Using Hard X-ray Photoelectron Spectroscopy. *Chem. Mater.* **20**, 4156–4160 (2008).
34. Bayer, B. C. *et al.* In Situ Observations of Phase Transitions in Metastable Nickel (Carbide)/Carbon Nanocomposites. *J. Phys. Chem. C* **120**, 22571–22584 (2016).
35. Cui, Y. *et al.* Tungsten Oxide/Carbide Surface Heterojunction Catalyst with High Hydrogen Evolution Activity. *ACS Energy Lett.* **5**, 3560–3568 (2020).
36. Li, H. *et al.* Operando Unveiling of Hydrogen Spillover Mechanisms on Tungsten Oxide Surfaces. *J. Am. Chem. Soc.* **147**, 6472–6479 (2025).
37. Xu, K. *et al.* Catalytically efficient Ni-NiO_x-Y_2O_3 interface for medium temperature water-gas shift reaction. *Nat. Commun.* **13**, 2443 (2022).
38. Mansour, A. N. Characterization of NiO by XPS. *Surf. Sci. Spectra* **3**, 231–238 (1994).
39. Duan, M. *et al.* Synergizing Inter and Intraband Transitions in Defective Tungsten Oxide for

Efficient Photocatalytic Alcohol Dehydration to Alkenes. *JACS Au* **2**, 1160–1168 (2022).

40. Ahmadi, M. *et al.* WO_3 nano-ribbons: their phase transformation from tungstite ($WO_3 \cdot H_2O$) to tungsten oxide (WO_3). *J. Mater. Sci.* **49**, 5899–5909 (2014).
41. Liu, F., Chen, X., Xia, Q., Tian, L. & Chen, X. Ultrathin tungsten oxide nanowires: oleylamine assisted nonhydrolytic growth, oxygen vacancies and good photocatalytic properties. *RSC Adv.* **5**, 77423–77428 (2015).
42. Dupin, J.-C., Gonbeau, D., Vinatier, P. & Levasseur, A. Systematic XPS studies of metal oxides , hydroxides and peroxides. *Phys. Chem. Chem. Phys.* **2**, 1319-1324 (2000).
43. Chen, Z. *et al.* Eutectoid-structured WC/W_2C heterostructures: A new platform for long-term alkaline hydrogen evolution reaction at low overpotentials. *Nano Energy* **68**, 104335 (2020).
44. Gabrusenoks, J., Veispals, A., Von Czarnowski, A. & Meiwes-Broer, K.-H. Infrared and Raman spectroscopy of WO_3 and $CdWO_4$. *Electrochimica Acta* **46**, 2229–2231 (2001).
45. Daniel, M. F., Desbat, B. & Lassegues, C. Infrared and Raman study of WO_3 tungsten trioxides and WO_3, xH_2O tungsten trioxide tydrates. *J. Solid State Chem.* **67**, 235–247 (1987).
46. Gomez, A., Piskulich, Z. A., Thompson, W. H. & Laage, D. Water Diffusion Proceeds via a Hydrogen-Bond Jump Exchange Mechanism. *J. Phys. Chem. Lett.* **13**, 4660–4666 (2022).
47. Sun, Q. *et al.* Understanding hydrogen electrocatalysis by probing the hydrogen-bond network of water at the electrified Pt–solution interface. *Nat. Energy* **8**, 859–869 (2023).
48. Yang, C., Fontaine, O., Tarascon, J.-M. & Grimaud, A. Chemical Recognition of Active Oxygen Species on the Surface of Oxygen Evolution Reaction Electrocatalysts. *Angew. Chem. Int. Ed.* **56**, 8652–8656 (2017).
49. Wang, H. *et al.* Breaking hydrogen bond network enhances oxygenic photosynthesis of photosystem II. *Fundam. Res.* S2667325825001190 (2025) doi:10.1016/j.fmre.2025.03.011.
50. Li, P. *et al.* Hydrogen bond network connectivity in the electric double layer dominates the kinetic pH effect in hydrogen electrocatalysis on Pt. *Nat. Catal.* **5**, 900–911 (2022).
51. Chen, X. *et al.* Tuning the Hydrogen Bond Network Inside the Helmholtz Plane for Industrial Hydrogen Evolution. *Adv. Funct. Mater.* **35**, 2503701 (2025).

52. Klassen, B., Aroca, R. & Nazri, G. A. Lithium Perchlorate: Ab Initio Study of the Structural and Spectral Changes Associated with Ion Pairing. *J. Phys. Chem.* **100**, 9334–9338 (1996).
53. Xuan, X., Wang, J., Tang, J., Qu, G. & Lu, J. A Vibrational Spectroscopic Study of Ion Solvation in Lithium Perchlorate/Propylene Carbonate Electrolyte. *Phys. Chem. Liq.* **39**, 327–342 (2001).
54. Li, Y. *et al.* Application of distribution of relaxation times method in polymer electrolyte membrane water electrolyzer. *Chem. Eng. J.* **451**, 138327 (2023).
55. Giesbrecht, P. K. & Freund, M. S. Investigation of Water Oxidation at IrO_2 Electrodes in Nafion-Based Membrane Electrode Assemblies Using Impedance Spectroscopy and Distribution of Relaxation Times Analysis. *J. Phys. Chem. C* **126**, 17844–17861 (2022).
56. Ran, P. *et al.* Disordered Ru–O_6 Octahedrons for Efficient and Selective Electro-oxidation of Sulfide to Sulfoxide via Boosted Surface Oxygen Kinetics. *J. Am. Chem. Soc.* **147**, 26254–26266 (2025).
57. Zaki, M. I., Mekhemer, G. A. H., Fouad, N. E. & Rabee, A. I. M. Structure–acidity correlation of supported tungsten(VI)-oxo-species: FT-IR and TPD studies of adsorbed pyridine and catalytic decomposition of 2-propanol. *Appl. Surf. Sci.* **308**, 380–387 (2014).
58. Fishman, A. I., Klimovitskii, A. E., Skvortsov, A. I. & Remizov, A. B. The vibrational spectra and conformations of ethylbenzene. *Spectrochim. Acta. A. Mol. Biomol. Spectrosc.* **60**, 843–853 (2004).
59. Wang, J., Qiu, X., Wang, Y., Zhang, S. & Zhang, B. Vibrational Spectra and Quantum Calculations of Ethylbenzene. *Chin. J. Chem. Phys.* **25**, 526–532 (2012).
60. Tope, B. B. *et al.* Catalytic mechanism of the dehydrogenation of ethylbenzene over Fe–Co/Mg(Al)O derived from hydrotalcites. *Appl. Catal. Gen.* **407**, 118–126 (2011).
61. Kato, S., Iwase, K., Harada, T., Nakanishi, S. & Kamiya, K. Aqueous Electrochemical Partial Oxidation of Gaseous Ethylbenzene by a Ru-Modified Covalent Triazine Framework. *ACS Appl. Mater. Interfaces* **12**, 29376–29382 (2020).
62. Wilsey, M. K. *et al.* Selective Toluene Electrooxidation to Benzyl Alcohol. *J. Am. Chem. Soc.*

147, 36117–36135 (2025).

63. Xiong, P. *et al.* Site-selective electrooxidation of methylarenes to aromatic acetals. *Nat. Commun.* **11**, 2706 (2020).
64. Ciucci, F. & Chen, C. Analysis of Electrochemical Impedance Spectroscopy Data Using the Distribution of Relaxation Times: A Bayesian and Hierarchical Bayesian Approach. *Electrochimica Acta* **167**, 439–454 (2015).
65. Wan, T. H., Saccoccio, M., Chen, C. & Ciucci, F. Influence of the Discretization Methods on the Distribution of Relaxation Times Deconvolution: Implementing Radial Basis Functions with DRTtools. *Electrochimica Acta* **184**, 483–499 (2015).
66. Chen, J., Quattrocchi, E., Ciucci, F. & Chen, Y. Charging processes in lithium-oxygen batteries unraveled through the lens of the distribution of relaxation times. *Chem* **9**, 2267–2281 (2023).
67. Kresse, G. & Furthmüller, J. Efficient iterative schemes for ab initio total-energy calculations using a plane-wave basis set. *Phys. Rev. B* **54**, 11169–11186 (1996).
68. Kresse, G. & Furthmüller, J. Efficiency of ab-initio total energy calculations for metals and semiconductors using a plane-wave basis set. *Comput. Mater. Sci.* **6**, 15–50 (1996).
69. Perdew, J. P., Burke, K. & Ernzerhof, M. Generalized Gradient Approximation Made Simple. *Phys. Rev. Lett.* **77**, 3865–3868 (1996).
70. Grimme, S., Ehrlich, S. & Goerigk, L. Effect of the damping function in dispersion corrected density functional theory. *J. Comput. Chem.* **32**, 1456–1465 (2011).
71. Grimme, S., Antony, J., Ehrlich, S. & Krieg, H. A consistent and accurate ab initio parametrization of density functional dispersion correction (DFT-D) for the 94 elements H-Pu. *J. Chem. Phys.* **132**, 154104 (2010).
72. McGrath, M. J. *et al.* Toward a Monte Carlo program for simulating vapor–liquid phase equilibria from first principles. *Comput. Phys. Commun.* **169**, 289–294 (2005).
73. Goedecker, S., Teter, M. & Hutter, J. Separable dual-space Gaussian pseudopotentials. *Phys. Rev. B* **54**, 1703–1710 (1996).

74. Hartwigsen, C., Goedecker, S. & Hutter, J. Relativistic separable dual-space Gaussian pseudopotentials from H to Rn. *Phys. Rev. B* **58**, 3641–3662 (1998).
75. VandeVondele, J. & Hutter, J. Gaussian basis sets for accurate calculations on molecular systems in gas and condensed phases. *J. Chem. Phys.* **127**, 114105 (2007).
76. Evans, D. J. & Holian, B. L. The Nose–Hoover thermostat. *J. Chem. Phys.* **83**, 4069–4074 (1985).
77. Verlet, L. Computer ‘Experiments’ on Classical Fluids. I. Thermodynamical Properties of Lennard-Jones Molecules. *Phys. Rev.* **159**, 98–103 (1967).

Acknowledgements

This work was supported by Shanghai Science and Technology Committee (23XD1421800 for X.-H.L.), Shanghai Shuguang Program (21SG12 for X.-H.L.), State Key Laboratory of Synergistic Chem-Bio Synthesis (sklscbs202551 for X.-H.L.), and Shanghai Municipal Science and Technology Major Project (J.-S.C.).

Author Contributions

X.-H.L., B.-L.L. and X.L. designed the experiments. B.-L.L. planned and performed catalyst synthesis, conducted performance tests and analyzed data. B.-L.L. finished the theoretical calculation. D.-H. Y. contributed to the substrate scope section. Q.-Y.L. and S.-N.Z. helped to analyze the theoretical calculation. X.-H.L. and B.-L.L. cowrote the original manuscript. X.-H.L. and J.-S.C. oversaw all the research phases. All of the authors discussed the results and commented on the paper.

Competing Interests

The authors declare no competing interests.

Figure Captions

Figure 1. Structure of Ni/W$_2$C pre-catalysts. a The AC-HAADF-STEM image of Ni$_{1.6}$/W$_2$C pre-catalysts and corresponding STEM-EDS elemental mapping results of W Lα line and Ni Kα line. **b** The atomic resolution AC-HAADF-STEM image of Ni$_{1.6}$/W$_2$C pre-catalysts (the blue circles indicate Ni dopants). **c** The corresponding intensity profiles of line I and line II in Figure 1b. **d** The XPS spectra of W 4*f* and Ni 2*p* of Ni$_{1.6}$/W$_2$C pre-catalysts.

Figure 2. Oxygen transfer from water to C(sp^3)–H bonds for C–H oxidation. a Schematic illustration of oxygen transfer from water to benzylic C(sp^3)–H bonds. **b** Time-dependent yields of the electrocatalytic oxygen transfer process over 48 hours at the anode. The inset picture shows yields change from 0 to 0.8 hours. Reaction conditions: 1.8 V vs. Ag/AgCl, with a catalyst loading of 1mg/cm^2. **c** The catalyst loading-dependent yields of oxygenated products and corresponding Faradaic efficiencies at 2.0 V vs. Ag/AgCl. **d** The potential-dependent yields of oxygenated products and corresponding Faradaic efficiencies with a catalyst loading of 1.5 mg/cm^2. **e** GC spectra of the electrolyte after oxidation with $H_2^{18}O$ at different reaction times. Anisole (at the retention time of 4.6 min) was used as the internal standard for quantification. **f-g** The mass spectrum of 1-phenylethanol and acetophenone generated at the anode using $H_2^{18}O$ as the oxygen source in 4 hours.

Figure 3. *In-situ* formation of highly active Ni-WOC sites. a The AC-HAADF-STEM image of the used Ni$_{1.6}$/W$_2$C pre-catalysts. **b** The AC-HAADF-STEM image and corresponding STEM-EDS mapping results of the used Ni$_{1.6}$/W$_2$C pre-catalysts. **c** The atomic-resolved AC-HAADF-STEM image of the used Ni$_{1.6}$/W$_2$C pre-catalysts. **d** The corresponding intensity profiles of line I and line II in Figure 3c. **e** Schematic illustration of *in-situ* formation of highly active Ni-WOC sites. **f-h** Fitted curves of time-dependent *ex-situ* XPS spectra of O 1*s*, Ni 2*p*, and W 4*f* obtained under 1.8 V versus Ag/AgCl, respectively **i** Yields of ethylbenzene oxygenation using different types of catalysts (reaction conditions: 1.8 V versus Ag/AgCl, with a catalyst loading of 1mg/cm^2).

Figure 4. Ni heteroatoms regulate interfacial water structure over the Ni-WOC for boosted oxygen species diffusion. a The equilibrium configuration of interfacial water structure and H-bond network over the Ni-WOC model revealed by AIMD simulation. **b** The calculated number

of hydrogen bonds over the dopant site of WOC and Ni-WOC models, respectively. **c** The calculated RDFs between water and surface dopant sites of WOC and Ni-WOC models, respectively. g(r) indicates the radical distribution function and r indicates the distances between water molecules and dopant sites. **d** Time-resolved ATR-SEIRAS spectra of water structure collected at 2.0 V versus Ag/AgCl on WOC and Ni-WOC-based anode, respectively. **e-f** Potential-dependent DRT spectra of WOC and Ni-WOC-based anode, respectively. **g** Schematic illustration of oxygen diffusion from bulk liquid to Ni-WOC surface through the broken H-bond network caused by Ni heteroatoms.

Figure 5. The mechanism of regulated pathways for oxygen transfer from water to C(sp^3)–H bonds via Ni-WOC. **a** Schematic illustration of absorbed water at site 1. **b** The adsorption energy of water at Ni and surrounding W sites of the Ni-WOC model. **c-d** The mass spectra of products obtained by using D_2O on Ni-WOC-based anodes and using H_2O on ^{18}O-labeled Ni-WOC-based anodes, respectively. **e-g** Potential-dependent *in-situ* ATR-SEIRAS spectra of oxygen transfer process from 0.2 V to 2.4 V (vs. Ag/AgCl) on WOC-based and Ni-WOC-based anodes, respectively. **h-j** Potentiostatic *in-situ* ATR-SEIRAS spectra of oxygen transfer process before and after the addition of ethylbenzene at 2.0 V (vs. Ag/AgCl) on Ni-WOC-based anodes. **k** The Gibbs free energy profile and schematic illustration of OER pathways on WOC and Ni-WOC model, and oxygen transfer pathway on Ni-WOC model.

Figure 6. The advantages of Ni-WOC-based anode for oxygen transfer from water to different kinds of benzylic C(sp^3)–H bonds. **a** Yields and Faradaic efficiencies for oxygenated products of different kinds of benzylic C(sp^3)–H bonds over Ni-WOC-based anode. **b** The durability test for the Ni-WOC-based anode was performed with each cycle of 2 hours. **c** Oxygenation performance of the electrocatalytic systems for benzylic oxidation over Ni-WOC-based anode. Reaction conditions: 2.0 V versus Ag/AgCl, with a catalyst loading of 1.5 mg/cm^2.

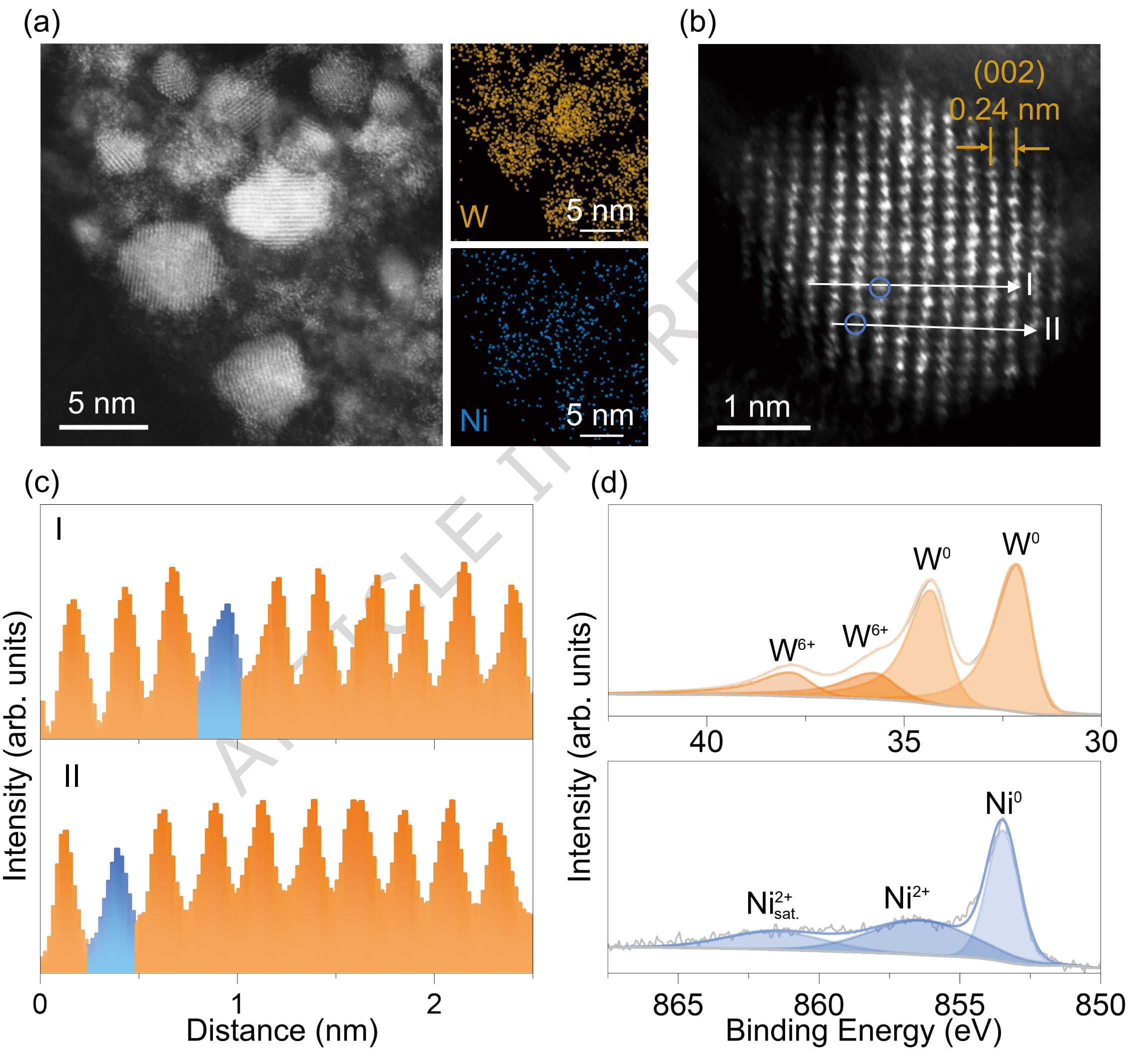
(a)
5 nm
W
5 nm
Ni
5 nm
(b)
(002)
0.24 nm
I
II
1 nm
(c)
I
II
Intensity (arb. units)
0
1
2
Distance (nm)
(d)
W0
W0
W6+
W6+
40
35
30
Ni0
Ni2+
Ni2+sat.
865
860
855
850
Binding Energy (eV)
Intensity (arb. units)

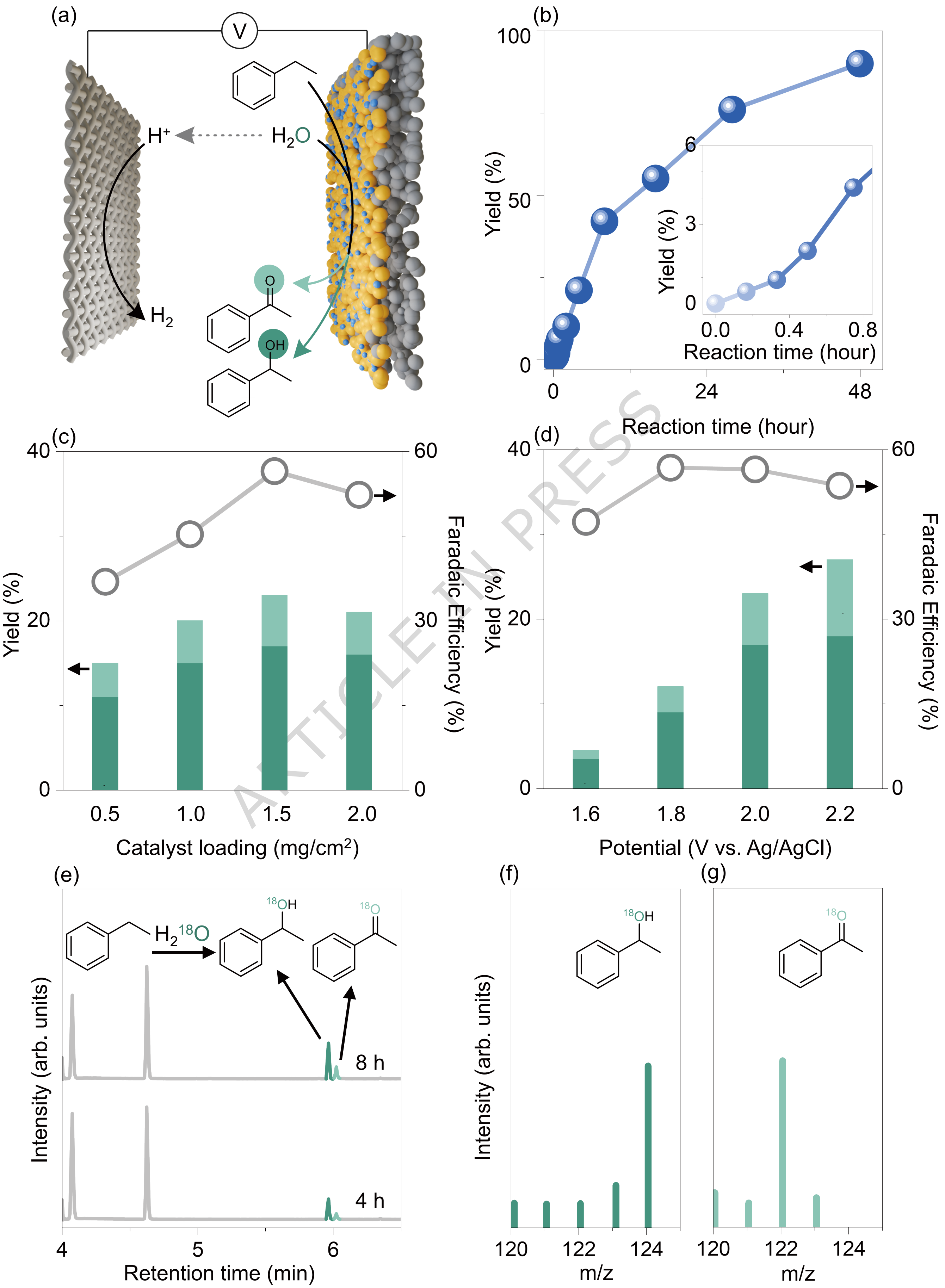
(a)
V
H⁺
H₂O
H₂
O
OH
(b)
Yield (%)
100
50
0
0
24
48
Reaction time (hour)
6
3
0
0.0
0.4
0.8
Yield (%)
Reaction time (hour)
(c)
Yield (%)
40
20
0
Faradaic Efficiency (%)
60
30
0
0.5
1.0
1.5
2.0
Catalyst loading (mg/cm²)
(d)
Yield (%)
40
20
0
Faradaic Efficiency (%)
60
30
0
1.6
1.8
2.0
2.2
Potential (V vs. Ag/AgCl)
(e)
H₂¹⁸O
¹⁸OH
¹⁸O
8 h
4 h
Intensity (arb. units)
4
5
6
Retention time (min)
(f)
¹⁸OH
Intensity (arb. units)
120
122
124
m/z
(g)
¹⁸O
120
122
124
m/z

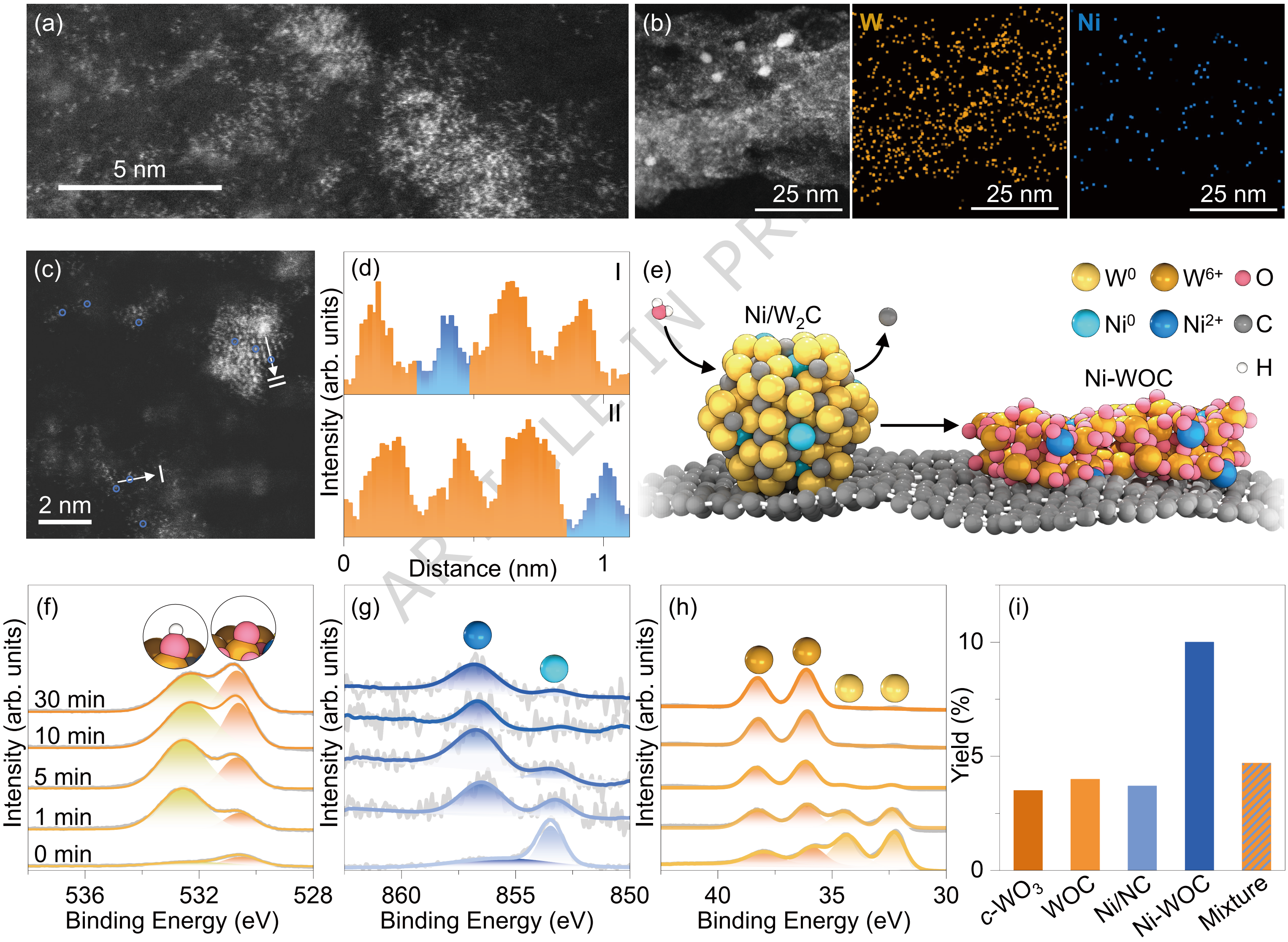
(a)
5 nm
(b)
25 nm
W
25 nm
Ni
25 nm
(c)
II
I
2 nm
(d)
I
II
Intensity (arb. units)
0
Distance (nm)
1
(e)
W^0
W^{6+}
O
Ni^0
Ni^{2+}
C
H
Ni/W_2C
Ni-WOC
(f)
30 min
10 min
5 min
1 min
0 min
Intensity (arb. units)
536
532
528
Binding Energy (eV)
(g)
Intensity (arb. units)
860
855
850
Binding Energy (eV)
(h)
Intensity (arb. units)
40
35
30
Binding Energy (eV)
(i)
Yield (%)
0
5
10
$c\text{-}WO_3$
WOC
Ni/NC
Ni-WOC
Mixture

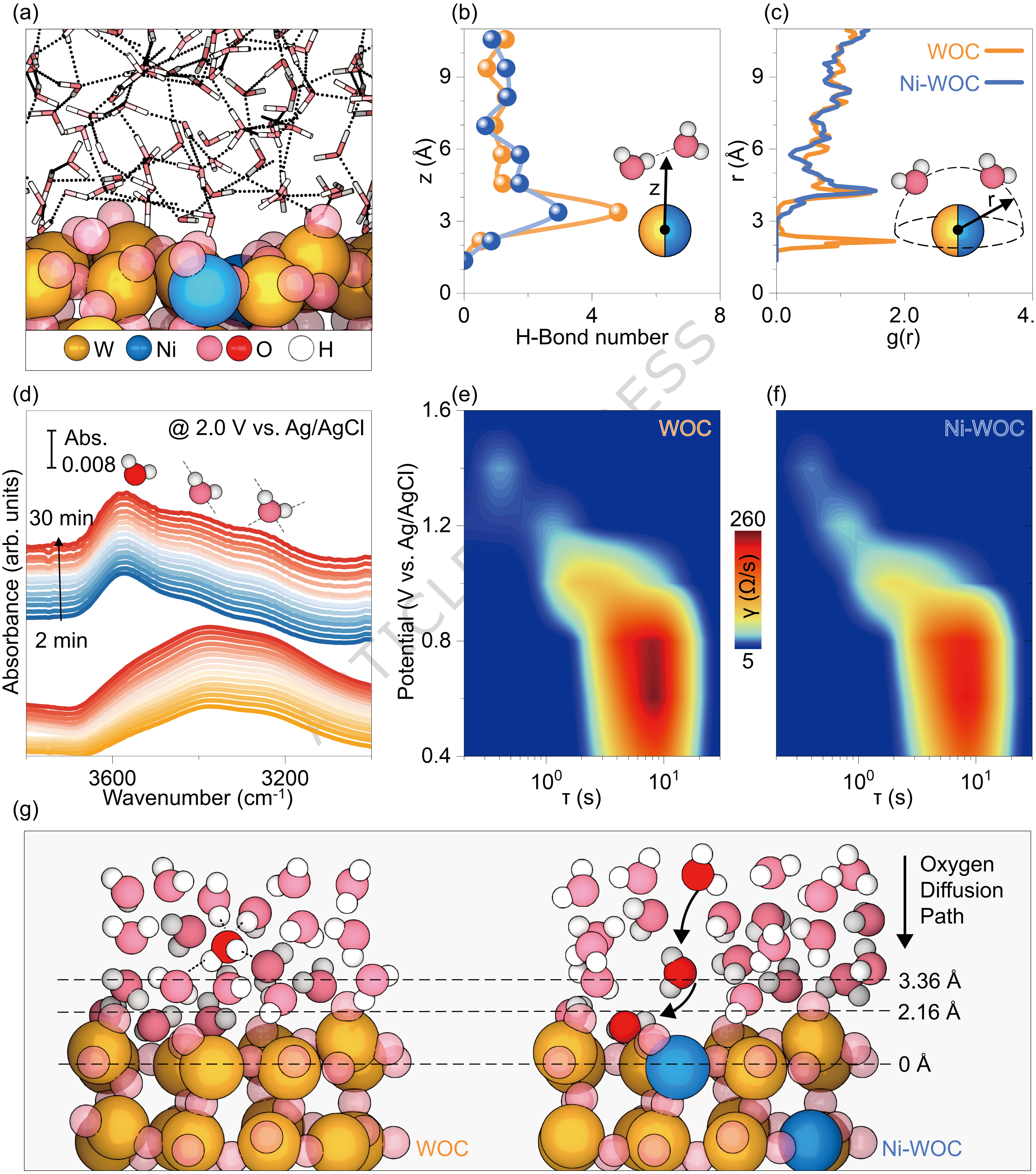
(a)
W
Ni
O
H
(b)
z (Å)
H-Bond number
z
0
3
6
9
0
4
8
(c)
r (Å)
g(r)
WOC
Ni-WOC
r
0.0
2.0
4.0
(d)
Abs. 0.008
@ 2.0 V vs. Ag/AgCl
30 min
2 min
Absorbance (arb. units)
Wavenumber (cm^{-1})
3600
3200
(e)
WOC
Potential (V vs. Ag/AgCl)
1.6
1.2
0.8
0.4
10^0
10^1
τ (s)
260
γ (Ω/s)
5
(f)
Ni-WOC
10^0
10^1
τ (s)
(g)
Oxygen Diffusion Path
3.36 Å
2.16 Å
0 Å
WOC
Ni-WOC

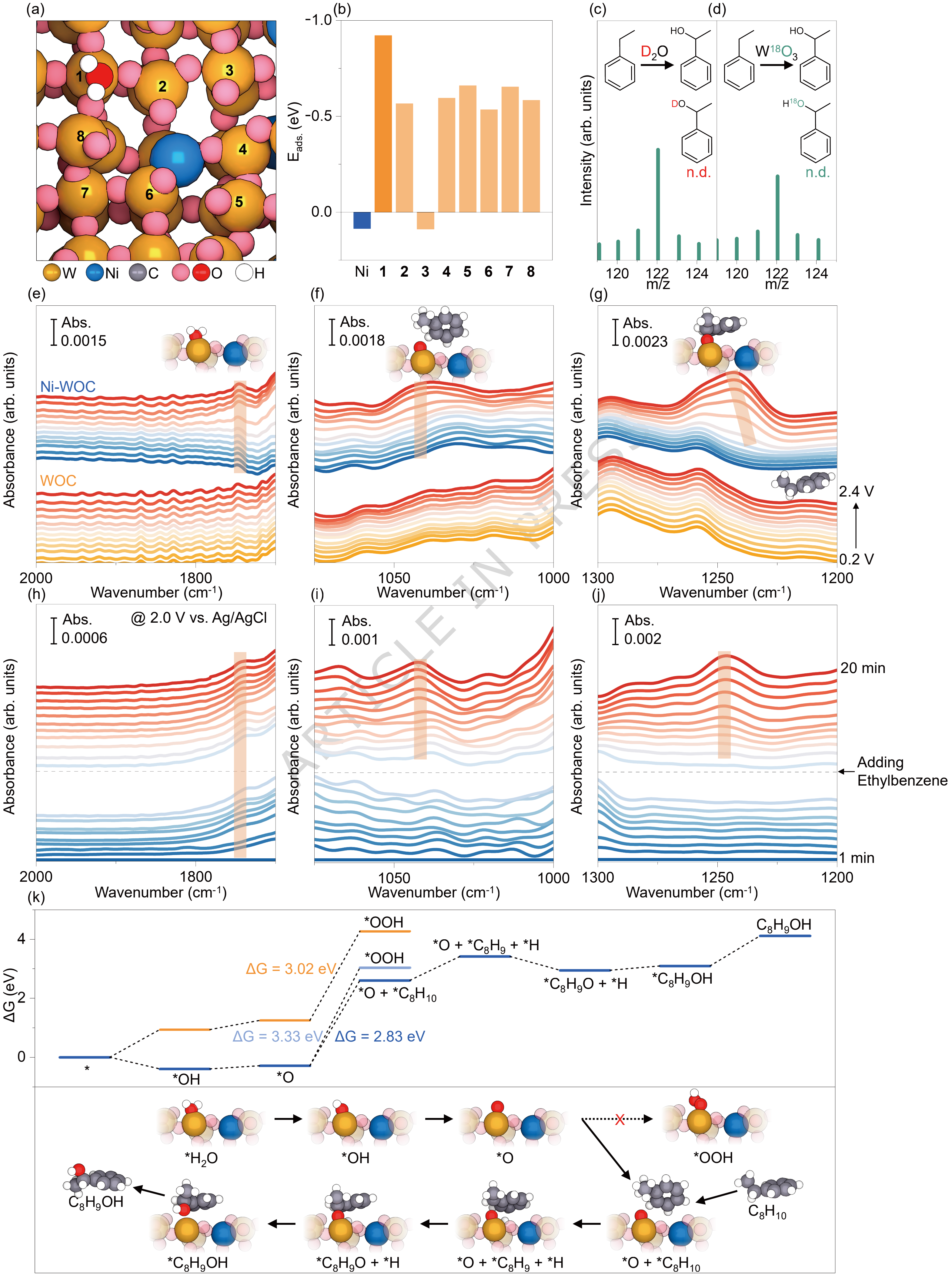
(a)
1
2
3
4
5
6
7
8
W
Ni
C
O
H
(b)
$E_{ads.}$ (eV)
-1.0
-0.5
0.0
Ni 1 2 3 4 5 6 7 8
(c)
(d)
Intensity (arb. units)
D_2O
HO
DO
n.d.
$W^{18}O_3$
$H^{18}O$
n.d.
120 122 124
m/z
(e)
(f)
(g)
Abs. 0.0015
Abs. 0.0018
Abs. 0.0023
Ni-WOC
WOC
Absorbance (arb. units)
2.4 V
0.2 V
2000 1800
1050 1000
1300 1250 1200
Wavenumber (cm^{-1})
(h)
(i)
(j)
Abs. 0.0006
@ 2.0 V vs. Ag/AgCl
Abs. 0.001
Abs. 0.002
20 min
Adding Ethylbenzene
1 min
(k)
ΔG (eV)
0
2
4
*
*OH
*O
*OOH
*OOH
ΔG = 3.02 eV
ΔG = 3.33 eV
ΔG = 2.83 eV
*O + *C_8H_{10}
*O + *C_8H_9 + *H
*C_8H_9O + *H
*C_8H_9OH
C_8H_9OH
*H_2O
*OH
*O
*OOH
C_8H_{10}
*O + *C_8H_{10}
*O + *C_8H_9 + *H
*C_8H_9O + *H
*C_8H_9OH
C_8H_9OH

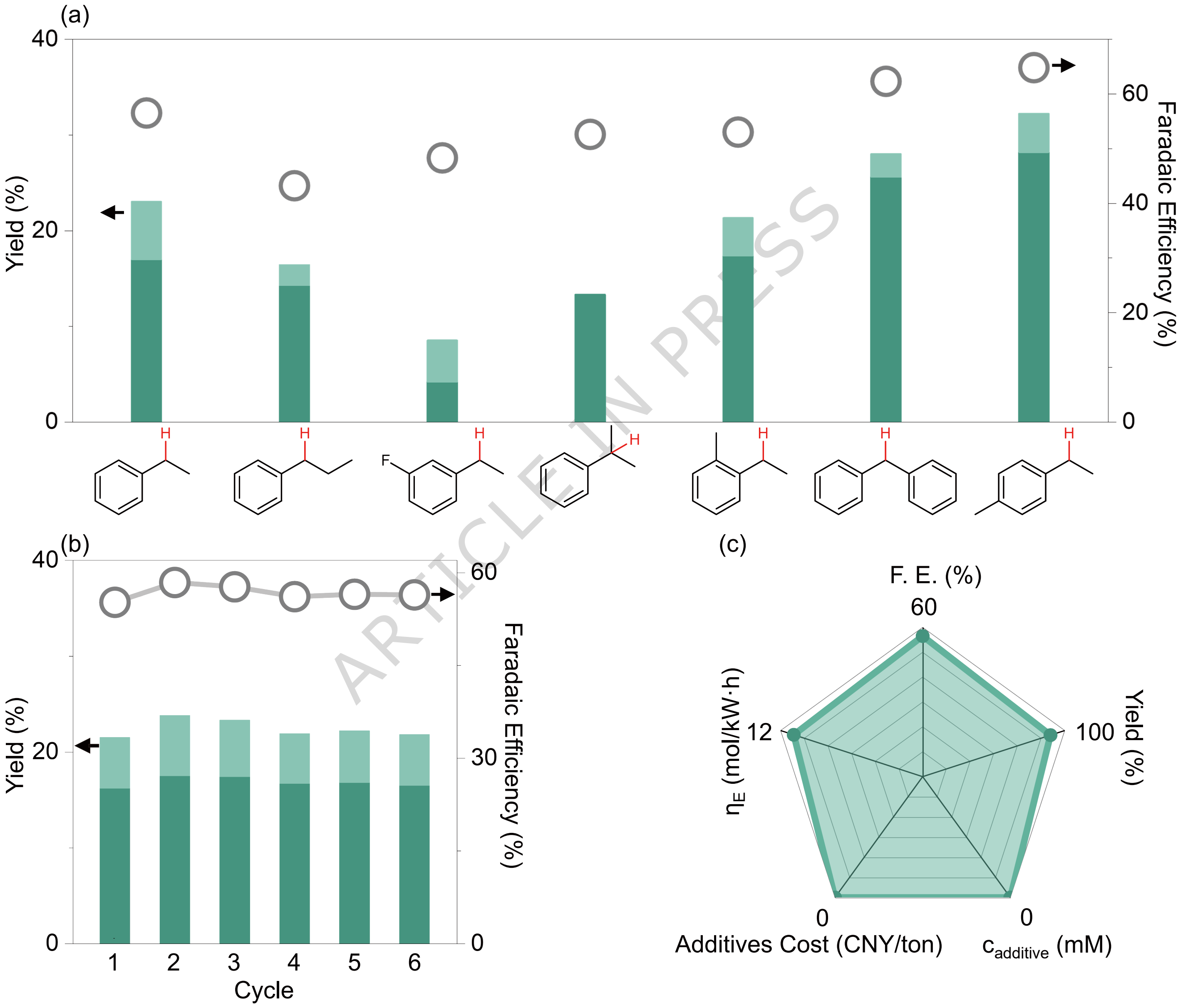
(a)
Yield (%)
0
20
40
Faradaic Efficiency (%)
0
20
40
60
H
F
(b)
Yield (%)
0
20
40
Faradaic Efficiency (%)
0
30
60
1
2
3
4
5
6
Cycle
(c)
F. E. (%)
60
Yield (%)
100
$c_{additive}$ (mM)
0
Additives Cost (CNY/ton)
0
η_E (mol/kW·h)
12